AGU PUBLICATIONS

JGR

Journal of Geophysical Research: Atmospheres

RESEARCH ARTICLE
10.1002/2014JD021500

**Key Points:**
- Used to identify local aerosol properties and sources
- Used to understand regional climate change

**Correspondence to:**
Z. Wang,
zzwang@aiofm.ac.cn

**Citation:**
Wang, Z., D. Liu, Z. Wang, Y. Wang, P. Khatri, J. Zhou, T. Takamura, and G. Shi (2014), Seasonal characteristics of aerosol optical properties at the SKYNET Hefei site (31.90°N, 117.17°E) from 2007 to 2013, *J. Geophys. Res. Atmos.*, *119*, 6128–6139, doi:10.1002/2014JD021500.

Received 15 JAN 2014
Accepted 24 APR 2014
Accepted article online 29 APR 2014
Published online 28 MAY 2014

# Seasonal characteristics of aerosol optical properties at the SKYNET Hefei site (31.90°N, 117.17°E) from 2007 to 2013

**Zhenzhu Wang[1], Dong Liu[1], Zhien Wang[1,2], Yingjian Wang[1,3], Pradeep Khatri[4], Jun Zhou[1], Tamio Takamura[4], and Guangyu Shi[5]**

[1]Key Laboratory of Atmospheric Composition and Optical Radiation, Anhui Institute of Optics and Fine Mechanics, Chinese Academy of Sciences, Hefei, China, [2]Department of Atmospheric Science, University of Wyoming, Laramie, Wyoming, USA, [3]University of Science and Technology of China, Hefei, China, [4]Center for Environmental Remote Sensing, Chiba University, Chiba, Japan, [5]Institute of Atmospheric Physics, Chinese Academy of Sciences, Beijing, China

**Abstract** Seasonal characteristics of aerosol optical properties in Sky Radiometer Network (SKYNET) Hefei site are studied using a sky radiometer from March 2007 to May 2013. The aerosol optical depth (AOD), Angstrom exponent (AE), volume size distributions, single-scattering albedo (SSA), refractive index, and asymmetry factor (ASY) of aerosols are simultaneously retrieved using the SKYRAD.pack version 4.2 software. During the study period, the AOD varied seasonally, with the maximum value of $1.02 \pm 0.42$ at 500 nm occurring in the summer, and the highest AOD ($1.13 \pm 0.42$) occurred in June due to stagnant climate conditions and accumulation of polluted aerosols before the East Asian summer monsoon. The variation in AE showed a different pattern, with the minimum ($0.97 \pm 0.28$) and maximum values ($1.30 \pm 0.22$) occurring during the spring and fall seasons, respectively. The relatively low value of AE in spring is related to the emission of Asian dust events. The aerosol volume size distributions can be expressed by the trimodal patterns for each season, consisting of a fine mode with $R < 0.6$ μm, a coarse mode with $R > 2.5$ μm, and a middle mode located between them. The real part of the refractive index increased with wavelength (380–870 nm) while the imaginary part of the refractive index decreased for all seasons except for the summer. The seasonal mean values of SSA were $0.97 \pm 0.02$ (summer), $0.95 \pm 0.03$ (spring), $0.93 \pm 0.04$ (autumn), and $0.91 \pm 0.04$ (winter) at 380 nm indicating more absorbing aerosol in the autumn and winter months. Furthermore, aerosol properties were greatly modified by condensation growth as evidenced by the positive dependencies of AOD, SSA, and ASY on relative humidity.

## 1. Introduction

Aerosols alter the radiative balance of the Earth atmosphere system by scattering and absorbing shortwave and longwave radiation directly [*Charlson et al.*, 1992]. Indirectly, aerosols can modify cloud microphysical properties and hence the radiative properties, amount, and lifetime of clouds, which will affect the climate [*Hansen et al.*, 1997; *Ramanathan et al.*, 2001a; *Lohmann and Feichter*, 2005; *Intergovernmental Panel on Climate Change* (*IPCC*), 2007]. The impact of aerosol on global and regional climate remains a high research priority [*IPCC*, 2007; *Ramanathan et al.*, 2008]. Despite a substantial increase in the efforts to further understand aerosols and their climatic effects [*Dubovik et al.*, 2002; *Nakajima et al.*, 2003; *Ramanathan et al.*, 2005; *Li et al.*, 2007a, 2011; *Xia et al.*, 2007a, 2007b; *Xin et al.*, 2007; *Lee et al.*, 2007; *Che et al.*, 2009a], considerable uncertainties still exist due to the large spatial and temporal variations of aerosol amount and properties and strong interactions of aerosols with other atmospheric processes [*IPCC*, 2001, 2007]. Therefore, it is necessary to quantitatively characterize the aerosol optical properties (AOP) in different regions of climatic significance, especially in eastern China, where high aerosol loading is common and can thus impact areas downwind through long-range transportation. This is evident from the global aerosol optical depth (AOD) distribution from Moderate Resolution Imaging Spectroradiometer (MODIS) [*Kaufman et al.*, 2002; *Kim et al.*, 2007].

Both in situ and remote sensing observations are required to further investigate AOP, as well as to validate satellite-based measurements and model simulations [*Kaufman et al.*, 2002; *Alados-Arboledas et al.*, 2008]. Ground-based active and passive remote sensing observations provide reliable and continuous column-integrated or vertically resolved aerosol particles properties in major aerosol source regions around the world. Ground-based measurements are necessary for validating aerosol products obtained from various

satellite sensors and for process-level studies [*Li et al*., 2007b]. As a consequence, several ground-based observation networks of aerosols have been established in order to understand and evaluate aerosol loading, optical properties, and their effects on climate, including the Aerosol Robotic Network [*Holben et al*., 1998, 2001], Sky Radiometer Network (SKYNET) [*Nakajima et al*., 2003], Photometrie pour le Traitement Operationnel de normalization Satellitaire [*Goloub et al*., 2008], Canadian Sunphotometer Network [*Bokoye et al*., 2001], Aerosol Ground Station Network [*O'Brien and Mitchell*, 2003], China Aerosol Remote Sensing Network [*Che et al*., 2009b], and so on.

Aerosols in the East Asia region have attracted considerable attention owing to their high concentration and the coexistence of dust, industrial pollutants, and biomass burning aerosols [*Lau et al*., 2008]. Several international aerosol-focused experiments have been conducted downstream of major aerosol emission regions in Asia such as Aerosol Characterization Experiment-Asia and Indian Ocean Experiment [*Huebert et al*., 2003; *Nakajima et al*., 2003; *Ramanathan et al*., 2001b]. A few campaigns, such as Atmospheric Brown Cloud (ABC) and ABC-East Asia Regional Experiment, are conducted along selected Asian source regions [*Ramanathan et al*., 2005; *Nakajima et al*., 2007; *Takamura et al*., 2008]. Moreover, the last two major aerosol observation projects within mainland of China were the East Asian Study of Tropospheric Aerosols: An International Regional Experiment and the East Asian Study of Tropospheric Aerosols and their Impact on Regional Climate [*Li et al*., 2007a, 2011]. Previous studies focused on observations at Xianghe (in north China as a downwind mixed aerosol region) [*Li et al*., 2007c], Lanzhou (in northwestern China as a dust source region) [*Huang et al*., 2008], Taihu (in eastern China as a downwind pollution region) [*Liu et al*., 2012], and Shouxian (also in eastern China as a downwind mixed aerosol region) [*Fan et al*., 2010]. Other than these sites, multiyear and multisensor observations are collected at the Hefei (31.90°N, 117.17°E) site [*Zhou et al*., 2002; *Wu et al*., 2011] close to Shouxian (32.56°N, 116.78°E), which is located in the Jiang-Huai Plain. In general, the Hefei site is located along the convergence zone of the eastern monsoon system where the moist southeasterly circulation driven by the subtropical high pressure in the western Pacific and the cold air from the north meets. As a result, a prolonged precipitation event occurs during the early summer season (so-called Meiyu). In addition, Hefei station is influenced by both anthropogenic and natural aerosols such as smoke from the burning of agricultural residues and windblown soil/dust particles. Since the end of 1990s, the Hefei station is designated as a super SKYNET site [*Nakajima et al*., 2007; *Zhou et al*., 2002] operated continuously to measure AOP, cloud optical properties, and surface radiation using a sky radiometer, a sky camera, a polarization lidar, a microwave radiometer, a nephelometer, and a set of broadband radiometers. Currently, it operates as a supersite for the China 973 (i.e., China's National Basic Research Program) aerosol-cloud-precipitation project together with Xianghe and Lanzhou stations. The long-term observations at the Hefei site offer an important data source to study regional climate change related to seasonal aerosol variations in China.

This paper presents results from the analysis of long-term AOP collected from 2007 to 2013 at Hefei using a ground-based sky radiometer, which is a key instrument of SKYNET. Brief descriptions of data collected and methods used in the analyses are given in section 2. Section 3 presents the seasonal characteristics of AOPs, and conclusions and summaries are discussed in section 4.

## 2. Data Set and Methodology

All measurements are collected at the Hefei site. The area surrounding the site is grassy and is surrounded by water. The nearest urban influence is 15 km, and therefore, the site is close enough to be influenced by local urban or rural aerosols depending on wind direction.

The sky radiometer (POM02, PREDE Co. Ltd.) is used to measure the direct and diffuse solar radiations within a 1.0° full field of view (FOV) every 10 min in the daytime. The radiometer has 11 channels with wavelengths of 315 nm, 340 nm, 380 nm, 400 nm, 500 nm, 675 nm, 870 nm, 940 nm, 1020 nm, 1627 nm, and 2200 nm [*Uchiyama et al*., 2005]. The sky radiance is measured at 24 predefined scattering angles with a minimum angle of about 3.0°. With the exception of the 315 nm (for $O_3$), 940 nm (for water vapor), and 1627 nm and 2200 nm (for cloud) wavelengths, the remaining seven channels are designed for aerosol measurements and are used to retrieve AOP over the Hefei site in this study.

The SKYRAD.pack version 4.2 software [*Nakajima et al*., 1996], which is normally used [*Kim et al*., 2005; *Liu et al*., 2008; *Che et al*., 2008] and recognized till now [*Khatri et al*., 2014], was used to retrieve aerosol optical

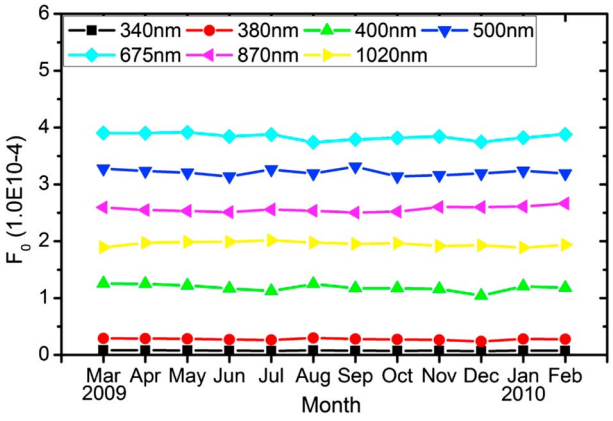


**Figure 1.** Monthly series of calibration constant $F_0$ for the sky radiometer using improved Langley method over Hefei from March 2009 to February 2010.

depth (AOD), single-scattering albedo (SSA), asymmetry parameter (ASY), and refractive index and also volume size distribution by using a radiative transfer code as well as linear and nonlinear inversion schemes. Monthly means of the ozone concentration and wavelength-dependent surface reflectance over the Hefei site from the Total Ozone Mapping Spectrometer and MODIS products (1° × 1° grid) are used as the additional inputs.

The sky radiometer can be calibrated onsite for the solid view angle (SVA) (using scan data of solar disc) and the calibration constant ($F_0$) (using improved Langley method) [*Campanelli et al*., 2004, 2007]. Both SVA and $F_0$ were processed by carefully selecting very stable and clear sky days and following the recommended calibration procedures [*Nakajima et al*., 1996]. Cloud screening for the sky radiometer observation data is performed using an algorithm developed by *Khatri and Takamura* [2009]. A sensitivity analysis of retrieved AOP from sky radiation measurements using SKYRAD.pack software is given by *Kim et al*. [2005] in detail. The accuracy with which AOD can be retrieved depends on mainly the accuracy value of $F_0$. Using the improved Langley method, a calibration accuracy of 1% can be achieved, and the errors in AOD are approximately 0.01. The volume size distributions, SSA, and refractive index can be retrieved with a reasonable high accuracy [*Kim et al*., 2005]. Although the retrieval pack is based on the assumption of spherical particle, the results of sky radiometer presented in this study are reliable enough to study the characteristics of aerosols including dust, because the calibration constants for direct irradiances were used in the analysis of aerosol optical parameters [*Kobayashi et al*., 2010; *Khatri et al*., 2014]. An intercomparison between a PREDE sky radiometer and a CIMEL Sun photometer is discussed in detail [*Che et al*., 2008]. On average, there is very small difference of AOD (<1.3%) and Angstrom exponent (AE) (<5.8%) for all wavelengths between PREDE sky radiometer and CIMEL Sun photometer measurements. However, *Che et al*. [2008] pointed out that the SSA values from the PREDE sky radiometer were slightly larger than those from CIMEL Sun photometer within 3% at 500–670 nm and 8% at 870–1020 nm. A good way to solve overestimation of SSA is to exclude so-called cirrus cloud contaminated data using a strict quality control algorithm [*Hashimoto et al*., 2012]; however, it may also exclude coarse dust aerosols. Since the dust aerosols commonly influence over the area [*Zhou et al*., 2002; *Wu et al*., 2011; *Liu et al*., 2011a, 2011b], the quality control algorithm does not apply in this study.

In order to verify the stabilization of the sky radiometer over Hefei, 1 year of data is selected and $F_0$ is calculated using SKYRAD.pack software. First, during each cloud-free day, one or two $F_0$ at each wavelength are obtained by using the improved Langley method [*Campanelli et al*., 2007]. Second, outliers are removed based on a running standard deviation of 10 consecutive data points from a raw time series of $F_0$. This step is repeated 3 times. Third, the screened time series of $F_0$ is smoothed by taking a running mean of three consecutive data points. Lastly, the monthly averaged $F_0$ is used as a key input parameter to retrieving AOP. As shown in Figure 1, the monthly series of $F_0$ for the sky radiometer is constant over Hefei. The variations of $F_0$ at 500 nm and 675 nm during this period are less than 1.69% and 1.53% as illustrated in Figure 1.

In order to validate the quality of the PREDE sky radiometer, data from the Anhui Institute of Optics and Fine Mechanics (AIOFM) Sun photometer and Raman lidar near (~0.5 km separation) the Hefei site are selected for comparison. These two instruments are developed by AIOFM. The AIOFM Sun photometer makes the direct spectral solar irradiance within a 1° FOV at eight wavelengths at 1050, 940, 860, 780, 670, 610, 520, and 400 nm. It is calibrated every half year during cloud-free conditions on the top of a mountain (such as Yellow Mountain, 1814 m mean sea level, located in the southern Anhui province) using the normal Langley plot method with the precision is better than 3%. The AODs at 675 nm retrieved by sky radiometer and measured by Sun photometer in clear sky are collected during 2008–2010. There are 2993 matched measurements

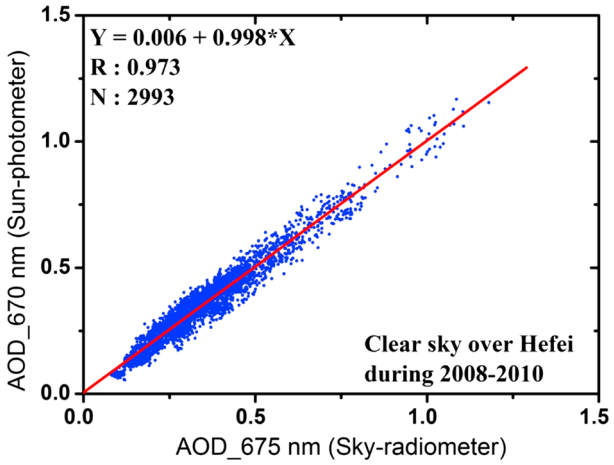


**Figure 2.** Scatterplot of simultaneous measurements of AOD between PREDE sky radiometer and AIOFM Sun photometer data at 675 nm.

within 2 min of each other for 125 days. Figure 2 shows the comparison result with a high correlation of 0.973 at 675 nm. The difference on average value between these two instruments at 675 nm is less than 1.41%, which indicates a high accuracy of retrieved AODs.

The AIOFM Raman lidar measurement employs a two-channel (532 nm Mie and 607 nm Raman) method [*Ansmann et al.*, 1992] to retrieve the aerosol lidar ratio (S1) in the nighttime and one channel (532 nm Mie) method [*Fernald*, 1984] to get aerosol extinction coefficient profiles for day and night. The Fernald method requires S1 as the inputs, and closed night time S1 is used for daytime retrievals. The AOD at 532 nm from Raman lidar is calculated from the profile of aerosol extinction coefficients. The AOD at 532 nm from the sky radiometer is derived from observed AOD at 500 nm and Angstrom exponent (AE) values at 340–1020 nm. Figure 3 shows a comparison based on 190 samples during 2009–2010 covering a wide variety of weather conditions from fine day, haze day, and dust day. The linear fitting results show a correlation coefficient of 94.3%.

## 3. Results and Discussion

Seasonal variations of AOP are investigated using 7 years (2007–2013) of radiometer measurements at the SKYNET Hefei site. During this period, 33,482 instantaneous retrievals of AOD, AE, SSA, ASY, refractive index, and volume size distribution are available for analysis over 1060 days. Seasons are defined as March-April-May (MAM: spring), June-July-August (JJA: summer), September-October-November (SON: autumn), and December-January-February (DJF: winter).

### 3.1. AOD and AE

Two important parameters are the AOD at 500 nm wavelength and the AE. The AE is derived from a multispectral log linear fit to AOD $\sim \lambda^{-AE}$ based on seven wavelengths in the range 340–1020 nm and can be considered as a first-order indicator of average aerosol size. Figure 4 shows monthly (a–c) and seasonal (d–f) average AOD at 500 nm and AE at 340–1020 nm for nearly 7 years (March 2007 to May 2013). The maximum monthly mean value of AOD occurs in June with the value of 1.13. The minimum monthly mean value of AOD which is 0.63 occurs in December. The results are in good agreement with the measurements at Taihu reported by *Yu et al.* [2011], where the high and low monthly average AODs at 500 nm are 1.17 in June and 0.58 in December, respectively. There is a distinct seasonal pattern from AOD: a relative steady AOD in the springtime, a striking increase to maximum AOD in the summer, a decrease to minimum in the fall and early winter, and again an increase to extremum in the late winter, which is similar to the results at Taihu [*Yu et al.*, 2011].

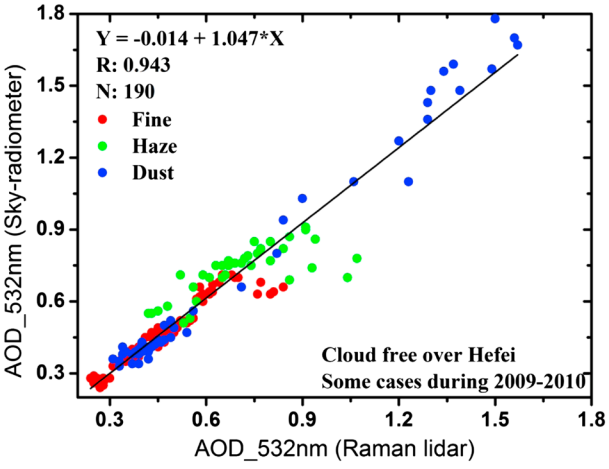


**Figure 3.** Comparison of AODs derived from PREDE sky radiometer and AIOFM Raman lidar at wavelength of 532 nm.

The annual mean AOD at 500 nm is 0.84, which is more than 8 times the minimum daily mean value (~0.10) observed at the site. The mean AOD here is slightly greater than observations in the other suburban

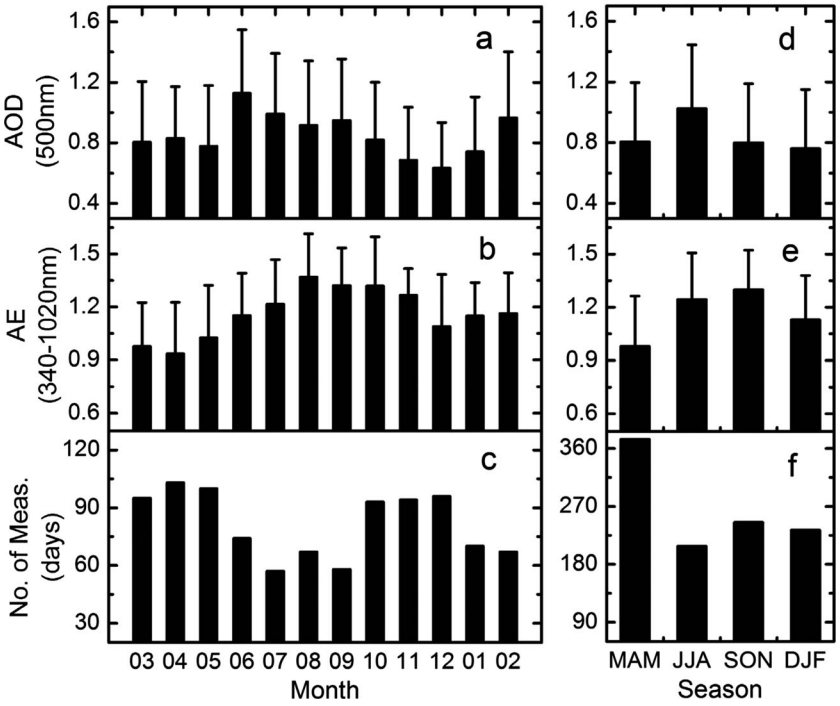


**Figure 4.** (a–c) Monthly and (d–f) seasonal means of AOD at 500 nm and AE at 340–1020 nm determined by the sky radiometer with a corresponding number of screened measurement days over the Hefei site from March 2007 to May 2013.

regions of eastern China, such as 0.77 and 0.75 at Taihu [*Xia et al*., 2007a; *Yu et al*., 2011] and 0.77 at Xianghe [*Li et al*., 2007c]. Heavy aerosol loading prevails all yearlong and the seasonal mean AODs at 500 nm are 0.80, 1.02, 0.80, and 0.76 in spring, summer, autumn, and winter, respectively.

The frequency distributions of daily mean AOD at 500 nm during the four seasons over Hefei are given in Figure 5. The number of samples analyzed for each season is 374, 208, 245, and 233 days respectively as shown in Figure 4. The frequency histogram of AOD indicates a wide range of AOD from ~0.1 to 2.2 and shows a significant seasonal variation with more frequent high AOD in summer than in the other seasons. The occurrences of AOD $<$ 0.5 are 24% (spring), 10% (summer), and 27% (autumn and winter). The occurrences of AOD between 0.5 and 1.0 are 50%, 39%, 46%, and 49% in spring, summer, autumn, and winter, respectively, while the occurrence of AOD $>$ 1.0 are 26%, 51%, 27%, and 24% for each season. This means that high AOD occurs year round at the Hefei site. The high values of AOD mainly occur in summer probably because of high temperature and high relative humidity during this season including hygroscopic growth. There is also an increase in fine-mode anthropogenic aerosols due to the convergence of local and transported pollution resulting from the presence of a stagnant weather system before summer monsoon over the eastern Asia continent [*Kim et al*., 2007; *Che et al*., 2009b; *Liu et al*., 2012].

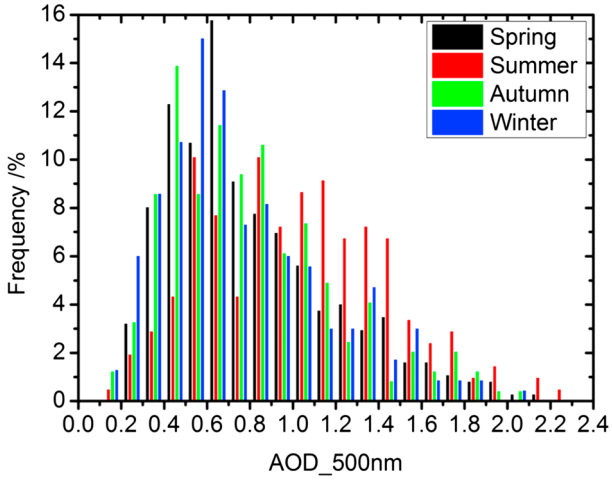


**Figure 5.** The frequency distributions of AOD at 500 nm for each season in the Hefei site.

Note that only seven daily mean AOD among a total 1060 daily means at this site are less than 0.20, which gives a percentage almost the same as that at the Taihu site [*Xia et al*., 2007a; *Liu et al*., 2012]

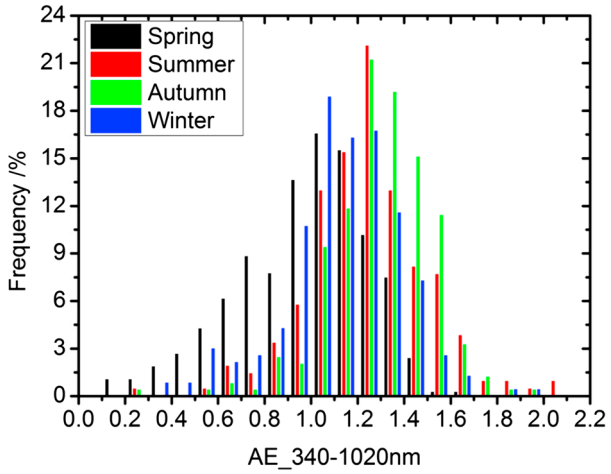


**Figure 6.** The frequency distributions of AE at 340–1020 nm for each season at the Hefei site.

but quite lower than 22% observed in the Xianghe site [*Xia et al*., 2007c]. These large differences are results of different weather and climate conditions among these sites. The Xianghe site is frequently influenced by cold airflow outbreaks, leading to a relatively high occurrence of background level aerosol loading [*Xia et al*., 2005, 2007c]. For the Hefei and Taihu sites in eastern China, the occurrences of cold airflow outbreaks are weaker than that in northern China. As previously mentioned, high temperature and relative humidity can promote the production of secondary aerosols and hygroscopic growth, causing AOD to increase in summer. The large amounts of precipitation at the Hefei and Taihu sites can cleanse the atmosphere through wet scavenging of aerosols during the rainy season. However, these low AOD situations are typically short lived due to high temperature and relative humidity in addition to local aerosol sources.

From Figure 4, the AE values over the Hefei site show a different season pattern than AOD with the lowest and highest monthly mean occurring in April and August. The annual mean AE is 1.13 while the seasonal means are 0.98, 1.24, 1.30, and 1.13 in spring, summer, fall, and winter, respectively. In spring, dust aerosols are transported out of northwest China and can affect aerosol loading and size over the Hefei site [*Zhou et al*., 2002; *Wu et al*., 2011], which leads to small AE values (large size). Dust aerosols can be transported to the region during winter but exhibit a much weaker influence. During summer and autumn, fine-mode pollution particles dominate the air over the Hefei site. The seasonal value here is very similar to the seasonal variation at Taihu with averages of 1.08 (1.09), 1.26 (1.26), 1.33 (1.31), and 1.22 (1.22) by *Yu et al*. [2011] and *Liu et al*. [2012], respectively. These variations will indicate signals of aerosol sources and their transportation. An influx of dust particles from the northern/northwest regions of China, carried in by winds associated with the Asian monsoon and continental anticyclones [*Tsai et al*., 2008; *Liu et al*., 2011b, 2012], is the likely cause for the relatively low springtime minimum.

Figure 6 shows the frequency distributions of AE at 340–1020 nm for each season at the Hefei site. The histograms of AE show a single modal structure centered at 1.0–1.1 in spring and winter and at 1.2–1.3 in summer and autumn. The AE ranges from 0.1 to 2.1, suggesting that there are different types of aerosol particles present (from very fine mode pollution to large coarse-mode dust). We define AE $<$ 0.5 as heavy dust events, 0.5 $<$ AE $<$ 1.0 as dust-affected anthropogenic aerosols, and AE $>$ 1.0 as fine-mode anthropogenic aerosols. We can see clear seasonal aerosol type variations in the region. During the spring season, approximately 47.3% of the AE values are smaller than 1.0 with 6.7% (25 days) within 0.1–0.5. The winter season has the second high occurrence of dust with 24.5% cases with AE less than 1.0 and 1.7% (4 days) cases with AE within 0.1–0.5. The region is less influenced by dust in the summer and fall with AE smaller than 1.0 less than 13.5% and 6.5%, respectively, and with 0.5% (1 day) having AE between 0.1 and 0.5. Therefore, annually, the site is dominated (~74%) by fine-mode pollutions with high occurrence of floating dust aerosols (~23%) and a few heavy dust cases (~3%).

Studies pointed out that variations of the relationship between AE and AOD might provide a possible way to identify and estimate the effects of different sources on aerosol loading and aerosol size for each season at different sites [*Cheng et al*., 2006; *Zheng et al*., 2008; *Che et al*., 2009c]. Figure 7 shows the relationship between AE and AOD for the four seasons at the Hefei site. In general, AE decreases with increasing AOD but with clear seasonal variations linked with local emission changes or long-range aerosol transport. The general negative relationship implies that high AODs often associate with large aerosol particles. Although hygroscopic growth due to the swelling effect is likely a major factor [*Eck et al*., 2005; *Li et al*., 2007a], frequent air mass stagnation episodes in summer (when relative humidity (RH) is high) may also contribute to this correlation. On the other hand, the size of fine-mode aerosols shifts to large ones due to enhanced coagulation with increasing aerosol loading. The relationships between AE and AOD at several other sites in northern China are

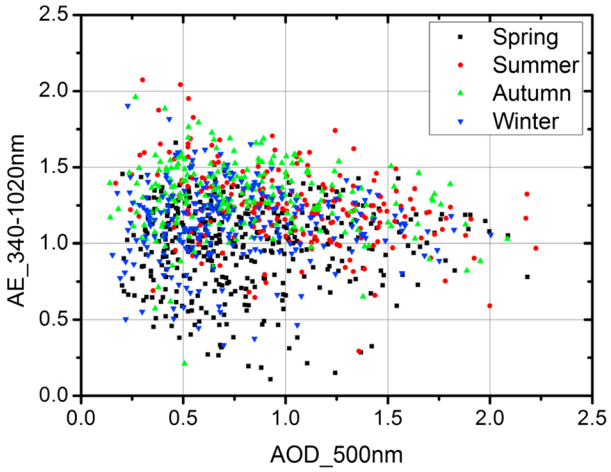


**Figure 7.** Relationship between the daily mean AE from 340–1020 nm and the daily mean AOD at 500 nm for each season at the Hefei site.

investigated by *Xia et al.* [2004], *Zheng et al.* [2008], *Cheng et al.* [2006], and *Li et al.* [2007c]. At the Dunhuang site, dust particles are the dominant sources, and the relationship can be characterized by an integrated exponential function. At the Xianghe, there is no obvious relationship between AE and AOD due to its complex aerosol sources.

### 3.2. Aerosol Size Distribution

The aerosol volume size distribution is determined using 20 bins ranging from 0.01 μm to 20 μm (0.01, 0.02, 0.03, 0.04, 0.06, 0.08, 0.12, 0.17, 0.25, 0.37, 0.54, 0.79, 1.16, 1.69, 2.47, 3.62, 5.29, 7.73, 11.31, and 16.54 μm). Figure 8 illustrates the seasonal variations of aerosol size distributions and mean size distributions for different AOD ranges. For each season and each AOD bin, the aerosol volume size distributions can be generally characterized by the trimodel patterns with a fine mode with a radius of less than 0.6 μm, a coarse mode with a radius of larger than 2.5 μm, and a middle mode located between the radius of 0.6 μm and 2.5 μm. The peak volumes of fine mode are 0.06 $\mu m^3/\mu m^2$ (spring), 0.10 $\mu m^3/\mu m^2$ (summer), 0.08 $\mu m^3/\mu m^2$ (autumn), and 0.06 $\mu m^3/\mu m^2$ (winter) at radius of 0.17 μm, 0.25 μm, 0.17 μm, and 0.17 μm, respectively. The coarse modes show the maxima at radius of 7.73 μm, 5.29 μm, and 5.29 μm in spring, autumn, and winter with peak volumes of 0.14 $\mu m^3/\mu m^2$, 0.08 $\mu m^3/\mu m^2$, and 0.11 $\mu m^3/\mu m^2$. The coarse mode in summer increased with increasing radius which is a jumped tail and is likely a result of cirrus cloud contamination [*Hashimoto et al.*, 2012]. An obvious middle mode in summer can be seen with peak volumes of 0.04 $\mu m^3/\mu m^2$ at the radius of 1.16 μm. The significant increase of coarse mode in springtime is mainly attributed to long-ranged transported dust. The increase in magnitude of the fine mode in summer season is related to the growth of hygroscopic and coagulation particles when the relative humidity and temperature are high.

Figure 8 also clearly indicates the positive dependencies of the volume concentration of fine, middle, and coarse modes on AOD, especially for the fine mode where the fine-mode radius shifts from 0.12 μm to 0.25 μm with peak volumes changing from 0.02 $\mu m^3/\mu m^2$ to 0.19 $\mu m^3/\mu m^2$ as well. The volume concentrations of fine mode for the last six AOD values are 9.2, 7.9, 6.0, 4.5, 3.1, and 1.9 times higher than that of the first AOD value, respectively. The increasing ratio of peak volumes on fine mode is more than that on coarse mode. Variations in aerosol volume size distributions are largely due to variable aerosol source regions.

### 3.3. Refractive Index

The real and imaginary parts of aerosol refractive indices, which are related to different chemical components, denote the aerosol scattering and absorption ability of incoming solar radiation, respectively.

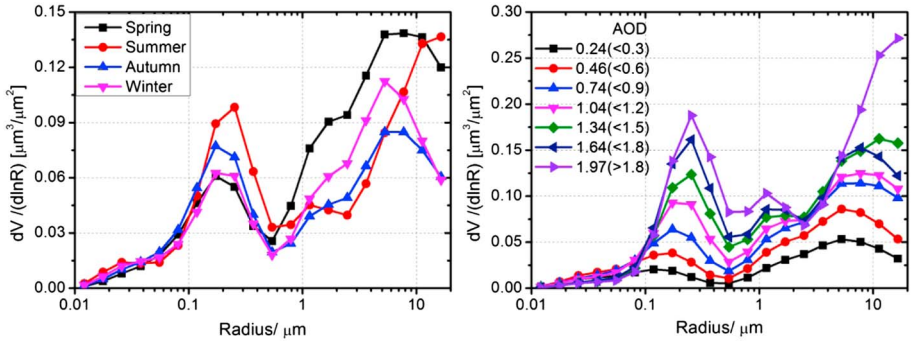


**Figure 8.** The average volume size distributions of aerosols as a function of particle radius at the Hefei site during 2007–2013 for (left) different seasons and (right) different AOD bins at 500 nm.

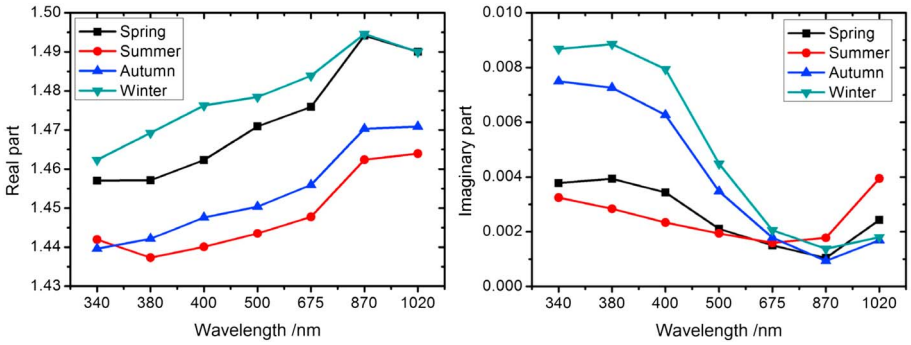


**Figure 9.** Seasonal averaged (left) real and (right) imaginary parts of aerosol refractive index at seven wavelengths.

Figure 9 shows the seasonal mean spectral values of the real and imaginary parts of aerosol refractive index retrieved at the Hefei site. The results show that real parts of the refractive index increase with wavelength from 380–870 nm because of stronger scattering in the near-infrared by coarse particles. There are also noticeable seasonal variations in the real parts with averages of 1.44 (summer), 1.45 (autumn), 1.47 (spring), and 1.48 (winter) at 500 nm.

Imaginary parts of the refractive index also decrease drastically from 380 to 870 nm except for summer season then increase slightly from 870 to 1020 nm for all seasons. That means the larger imaginary part in the shorter wavelengths suggests higher absorption by fine particle at the Hefei site. However, the imaginary part of the refractive index at 400 nm is larger in winter (0.0079) and autumn (0.0063) than that in spring (0.0034) and summer (0.0023).

### 3.4. SSA

The aerosol single-scattering albedo (SSA), defined as the ratio between the particle scattering coefficient and the total extinction coefficient, is typically used to characterize the aerosol absorption properties and is a key variable in assessing the radiative forcing due to aerosols. The SSA is mainly dependent on the chemical composition and size distribution of aerosol particles. The seasonal averages of SSA are shown in Figure 10, as well as the variations of SSA along AOD at 500 nm. As expected, the SSA shows an opposite wavelength dependence to the imaginary part of the refractive index with a significant increase in SSA from 380 to 870 nm except for the summer season and a slightly decreasing from 870 to 1020 nm for all seasons. The seasonal variations are presented with mean values of 0.98 (summer), 0.97 (spring), 0.96 (autumn), and 0.95 (winter) at 500 nm and of 0.97 (summer), 0.95 (spring), 0.93 (autumn), and 0.91 (winter) at 380 nm, respectively. The seasonal variation indicates more absorption of visible light in the winter and autumn months by fine-mode aerosol particles at the Hefei site. This result can be explained by the long-range transport of urban aerosols such as black carbon along with cold flow in winter from north/northeast China and local farm burning during the autumn harvest season. The annual mean single-scattering albedo was near 0.95 at 440 nm (interpolated approximately from the 400 nm and 500 nm wavelengths), which is higher

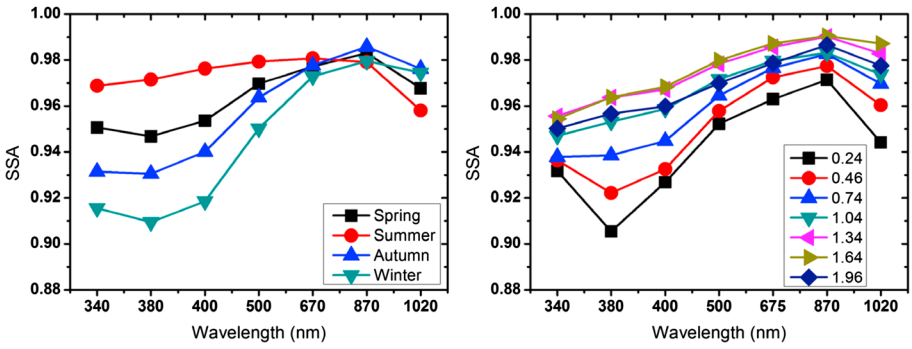


**Figure 10.** Mean spectral values of the SSA for (left) different seasons and (right) AOD bins at 500 nm observed at the Hefei site.

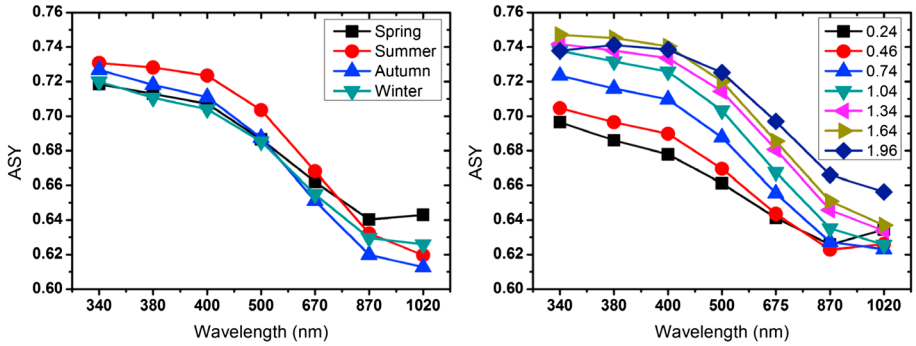


**Figure 11.** Mean spectral values of the ASY for (left) different seasons and (right) AOD bins (at 500 nm) at the Hefei site.

than those measured at the Taihu site (0.90 at 440 nm) [*Xia et al.*, 2007a; *Liu et al.*, 2012] and at Shouxian (0.92 at 440 nm) [*Fan et al.*, 2010], indicating less absorbing aerosols at the Hefei site.

The mean spectral SSAs from seven AOD bins (0.24, 0.46, 0.74, 1.04, 1.34, 1.64, and 1.96 at 500 nm) show increasing SSA with increasing AOD except for the SSA in the last two AOD bins. The SSA at the visible wavelengths is generally less but with stronger AOD dependence than that at the near-infrared wavelength. For example, the SSA at 380 nm varies from 0.91 for the AOD 0.24 bin to 0.96 for the AOD 1.64 bin; the SSA at 870 nm varies from 0.97 for the AOD 0.24 bin to 0.99 for the AOD 1.64 bin.

### 3.5. ASY

The asymmetry parameter represents the first moment of the particle scattering phase function. The values of asymmetry factor range from 0.1 under very clean conditions to 0.75 in the polluted situations under cloudless atmosphere [*Zege et al.*, 1991]. Figure 11 shows the seasonal mean spectral values of ASY and the ASY spectrum within seven AOD bins (at 500 nm) over the Hefei site. The ASY ranges from 0.61 to 0.73 with weak variations during all the seasons at a given wavelength. The seasonal mean ASYs generally decrease with wavelength increase for wavelength below 870 nm. However, the decreasing trend is smaller within 340–400 nm and 870–1020 nm than that in the range 400–870 nm. The results are similar to measurements at the Taihu site in spring [*Yu et al.*, 2006; *Liu et al.*, 2012], which may be related to the dust episodes in spring. In general, the mean spectral ASYs increase with AOD at 500 nm except for the ASY at 340–400 nm in 1.96 AOD bin and the ASY at 870–1020 nm in 0.24 and 0.46 bins.

As illustrated in Figures 10 and 11, both SSA and ASY increase along with increasing AOD. The amount of changes in SSA is noticeable, ranging from 0.02 to 0.05 over a range of AOD from 0.2 to 2.0. Meanwhile, the changes in ASYs vary from 0.04 to 0.07 over the same range. This can be related to the fine-mode particle size shift toward coarser with AOD increase as highlighted earlier (see Figure 8). These trends are observed in other regions (such as Taihu [*Xia et al.*, 2007a]) and are used as the base to model the dynamic changes of AOPs with aerosol loading [*Eck et al.*, 2005]. The positive dependence of fine-mode radius, the SSA, and the ASY on AOD may result from the mixed influence of the hygroscopic growth, coagulation growth, and variable species of aerosol emissions from various sources, such as coarse-mode airborne dust versus fine-mode anthropogenic pollution [*Li et al.*, 2007a]. For a fixed aerosol composition, the hygroscopic growth under humid environment should lead to the increase of fine-mode radius, thus enhanced

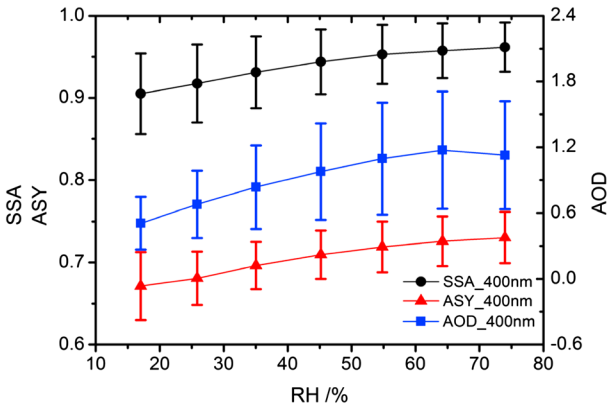


**Figure 12.** The dependence of AOD, ASY, and SSA at 400 nm on surface relative humidity based on data from March 2007 to May 2013 at the Hefei site; AOD, ASY, and SSA are averaged for seven RH bins ranging from 10% to 80%, and the vertical lines indicate standard deviation.

scattering (increasing the AOD), diminished aerosol absorption efficiency (increasing the SSA), and enlarged particle size (increasing the ASY) [*Xia et al*., 2007a]. This is confirmed with measurements at the Hefei site as illustrated in Figure 12, which show the positive dependencies of AOD, SSA, and ASY on relative humidity. This suggests that aerosol properties are greatly modified by condensation growth, which is also observed in the other region (such as Taihu [*Xu et al*., 2002]).

## 4. Conclusions

Using 7 years of ground-based sky radiometer remote sensing data, the seasonal AOPs at the Hefei site are investigated in detail. The major findings are listed below:

1. High aerosol loading exists in this region throughout the year, and the annual mean AOD at 500 nm equals to 0.84 varying from 0.76 (in winter) to 1.02 (in summer). High temperature and high relative humidity, as well as the presence of a stagnant weather system before the summer monsoon over the East Asia continent, led to higher AOD during the summer.
2. The annual mean AE is 1.13, and the seasonal mean AEs are 0.98, 1.24, 1.30, and 1.13 in spring, summer, fall, and winter, respectively. Annually, the site is dominated (~74%: AE $>$ 1) by fine-mode pollutants with high frequent occurrences of floating dust aerosols (~23%: 0.5 $<$ AE $<$ 1) and a few heavy dust cases (~3%: AE $<$ 0.5). Dust aerosols transported from the northern/northwest regions of China cause the relatively low springtime minimum of AE.
3. The aerosol volume size distributions can be generally characterized by the trimodal patterns with a fine mode ($R < 0.6$ μm), a coarse mode ($R > 2.5$ μm), and an intermediate mode (0.6 μm $< R <$ 2.5). The positive dependencies of the volume concentration of fine, middle, and coarse modes on AOD are shown. In terms of the fine mode, the center radius shifts from 0.12 μm to 0.25 μm with peak volumes changing from 0.02 $\mu m^3/\mu m^2$ to 0.19 $\mu m^3/\mu m^2$ as well. In essence, the size shift illustrates the general negative relationship between AOD and AE.
4. The seasonal mean spectral values of the real and imaginary parts of aerosol refractive index indicate stronger scattering by coarse particles and higher absorption by fine-mode particles at the Hefei site. The long-range transport of urban aerosol with black carbon in winter and the local farm burning during the autumn is responsible for the relatively low SSA.
5. Positive dependencies of AOD, SSA, and ASY on relative humidity indicate that aerosol properties are greatly modified by hygroscopic growth.

**Acknowledgments**
This research is supported by the Ministry of Science and Technology of China (2013CB955802), the Anhui Provincial Natural Science Foundation (1308085MD53), and the National Natural Science Foundation of China (41305022). We also thank the anonymous reviewers for their good comments.

## References

Alados-Arboledas, L., et al. (2008), Aerosol columnar properties retrieved from CIMEL radiometers during VELETA 2002, *Atmos. Environ.*, *42*, 2654–2667.

Ansmann, A., M. Riebesell, U. Wandinger, C. Weitkamp, E. Voss, W. Lahmann, and W. Michaelis (1992), Combined Raman elastic-backscatter lidar for vertical profiling of moisture, aerosol extinction backscatter, and lidar ratio, *Appl. Phys. B*, *55*, 18–28.

Bokoye, A. I., A. Royer, N. T. O'Neill, G. Fedosejevs, P. M. Teillet, and B. McArthur (2001), Characterization of atmospheric aerosols across Canada. Assessment from a ground-based Sun-photometer network: AEROCAN, *Atmos. Ocean*, *39*(4), 429–456.

Campanelli, M., T. Nakajima, and B. Olivieri (2004), Determination of the solar calibration constant for a Sun-Sky radiometer: Proposal of an in-situ procedure, *Appl. Opt.*, *43*, 651–659.

Campanelli, M., V. Estellés, C. Tomasi, T. Nakajima, V. Malvestuto, and J. A. Martínez-Lozano (2007), Application of the SKYRAD improved Langley plot method for the in situ calibration of CIMEL Sun-sky photometers, *Appl. Opt.*, *46*, 2688–2702.

Charlson, R. J., S. E. Schwartz, J. H. Hales, R. D. Cess, J. A. Coakley Jr., J. E. Hansen, and D. J. Hofmann (1992), Climate forcing by anthropogenic aerosols, *Science*, *255*, 423–430.

Che, H., G. Shi, A. Uchiyama, A. Yamazaki, H. Chen, P. Goloub, and X. Zhang (2008), Intercomparison between aerosol optical properties by a PREDE skyradiometer and CIMEL sunphotometer over Beijing, China, *Atmos. Chem. Phys.*, *8*, 3199–3214, doi:10.5194/acp-8-3199-2008.

Che, H., X. Zhang, S. Alfraro, B. Chatenet, L. Gomes, and J. Zhao (2009a), Aerosol optical properties and its radiative forcing over Yulin, China in 2001 and 2002, *Adv. Atmos. Sci.*, *26*(3), 564–576.

Che, H., et al. (2009b), Instrument calibration and aerosol optical depth validation of the China Aerosol Remote Sensing Network, *J. Geophys. Res.*, *114*, D03206, doi:10.1029/2008JD011030.

Che, H., Z. Yang, X. Zhang, C. Zhu, Q. Ma, H. Zhou, and P. Wang (2009c), Study on the aerosol optical properties and their relationship with aerosol chemical compositions over three regional background stations in China, *Atmos. Environ.*, *43*, 1093–1099, doi:10.1016/j.atmosenv.2008.11.010.

Cheng, T., H. Wang, Y. Xu, H. Li, and L. Tian (2006), Climatology of aerosol optical properties in northern China, *Atmos. Environ.*, *40*, 1495–1509.

Dubovik, O., B. Holben, T. F. Eck, A. Smirnov, Y. J. Kaufman, M. D. King, D. Tanré, and I. Slutsker (2002), Variability of absorption and optical properties of key aerosol types observed in worldwide locations, *J. Atmos. Sci.*, *59*, 590–608.

Eck, T. F., et al. (2005), Columnar aerosol optical properties at AERONET sites in central eastern Asia and aerosol transport to the tropical mid-Pacific, *J. Geophys. Res.*, *110*, D06202, doi:10.1029/2004JD005274.

Fan, X., H. Chen, X. Xia, Z. Li, and M. Cribb (2010), Aerosol optical properties from the Atmospheric Radiation Measurement Mobile Facility at Shouxian, China, *J. Geophys. Res.*, *115*, D00K33, doi:10.1029/2010JD014650.

Fernald, F. G. (1984), Analysis of atmospheric lidar observation: Some comments, *Appl. Opt.*, *23*, 652–653.

Goloub, P., et al. (2008), PHOTONS/AERONET sunphotometer network overview: Description, activities, results, in *Fourteenth International Symposium on Atmospheric and Ocean Optics/Atmospheric Physics*, Proceedings of the SPIE, vol. 6936, 69360 V-15, edited by G. G. Matvienko and V. A. Banakh, doi:10.1117/12.783171.

Hansen, J., M. Sato, and R. Ruedy (1997), Radiative forcing and climate response, *J. Geophys. Res.*, *102*, 6831–6864, doi:10.1029/96JD03436.

Hashimoto, M., T. Nakajima, O. Dubovik, M. Campanelli, H. Che, P. Khatri, T. Takamura, and G. Pandithurai (2012), Development of a new data-processing method for SKYNET sky radiometer observations, *Atmos. Meas. Tech.*, *5*, 2723–2737, doi:10.5194/amt-5-2723-2012.

Holben, B. N., et al. (1998), AERONET—A federated instrument network and data archive for aerosol characterization, *Remote Sens. Environ.*, *66*, 1–16.

Holben, B. N., et al. (2001), An emerging ground-based aerosol climatology: Aerosol optical depth from AERONET, *J. Geophys. Res.*, *106*, 12,067–12,097, doi:10.1029/2001JD900014.

Huang, J., P. Minnis, B. Chen, Z. Huang, Z. Liu, Q. Zhao, Y. Yi, and J. K. Ayers (2008), Long-range transport and vertical structure of Asian dust from CALIPSO and surface measurements during PACDEX, *J. Geophys. Res.*, *113*, D23212, doi:10.1029/2008JD010620.

Huebert, B. J., T. Bates, P. B. Russell, G. Shi, Y. J. Kim, K. Kawamura, G. Carmichael, and T. Nakajima (2003), An overview of ACE-Asia: Strategies for quantifying the relationships between Asian aerosols and their climatic impacts, *J. Geophys. Res.*, *108*(D23), 8633, doi:10.1029/2003JD003550.

Intergovernmental Panel on Climate Change (IPCC) (2001), *Climate Change 2001: The Scientific Basis-Contribution of Working Group I to the Third Assessment Report of the Intergovernmental Panel on Climate Change*, Cambridge Univ. Press, New York.

Intergovernmental Panel on Climate Change (IPCC) (2007), *Climate Change 2007: The Physical Science Basis. Contribution of Working Group I to the Fourth Assessment Report of the Intergovernmental Panel on Climate Change*, edited by S. Solomon, D. Qin, and M. Manning, Cambridge Univ. Press, Cambridge, U. K.

Kaufman, Y. J., D. Tanré, and O. Boucher (2002), A satellite view of aerosols in the climate system, *Nature*, *419*, 215–223.

Khatri, P., and T. Takamura (2009), An algorithm to screen cloud-affected data for sky radiometer data analysis, *J. Meteorol. Soc. Jpn.*, *87*(1), 189–204.

Khatri, P., T. Takamura, A. Shimizu, and N. Sugimoto (2014), Observation of low single scattering albedo of aerosols in the downwind of the East Asian desert and urban areas during the inflow of dust aerosols, *J. Geophys. Res. Atmos.*, *119*, 787–802, doi:10.1002/2013JD019961.

Kim, D.-H., B.-J. Sohn, T. Nakajima, and T. Takamura (2005), Aerosol radiative forcing over East Asia determined from ground-based solar radiation measurements, *J. Geophys. Res.*, *110*, D10S22, doi:10.1029/2004JD004678.

Kim, S. W., S. C. Yoon, J. Kim, and S. Y. Kim (2007), Seasonal and monthly variation of columnar aerosol optical properties over East Asia determined from multi-year MODIS, LIDAR, and AERONET sun/sky radiometer measurements, *Atmos. Environ.*, *41*, 1634–1651.

Kobayashi, E., A. Uchiyama, A. Yamazaki, and R. Kudo (2010), Retrieval of aerosol optical properties based on the spheroid model, *J. Meteorol. Soc. Jpn.*, *88*, 847–856.

Lau, K.-M., et al. (2008), The joint aerosol monsoon experiment: A new challenge for monsoon climate research, *Bull. Am. Meteorol. Soc.*, *89*, 369–383, doi:10.1175/BAMS-89-3-369.

Lee, K. H., Z. Li, M. S. Wong, J. Xin, Y. Wang, W. M. Hao, and F. Zhao (2007), Aerosol single scattering albedo estimated across China from a combination of ground and satellite measurements, *J. Geophys. Res.*, *112*, D22S15, doi:10.1029/2007JD009077.

Li, Z., et al. (2007a), Preface to special section on East Asian studies of tropospheric aerosols: An international regional experiment (EAST-AIRE), *J. Geophys. Res.*, *112*, D22S00, doi:10.1029/2007JD008853.

Li, Z., F. Niu, K.-H. Lee, J. Xin, W. M. Hao, B. Nordgren, Y. Wang, and P. Wang (2007b), Validation and understanding of MODIS aerosol products using ground-based measurements from the handheld sunphotometer network in China, *J. Geophys. Res.*, *112*, D22S07, doi:10.1029/2007JD008479.

Li, Z., et al. (2007c), Aerosol optical properties and their radiative effects in northern China, *J. Geophys. Res.*, *112*, D22S01, doi:10.1029/2006JD007382.

Li, Z., et al. (2011), East Asian studies of tropospheric aerosols and their impact on regional climate (EAST-AIRC): An overview, *J. Geophys. Res.*, *116*, D00K34, doi:10.1029/2010JD015257.

Liu, J., Y. Zheng, Z. Li, and R. Wu (2008), Ground-based remote sensing of aerosol optical properties in one city in northwest China, *Atmos. Res.*, *89*(1–2), 194–205.

Liu, J., Y. Zheng, Z. Li, and M. Cribb (2011a), Analysis of cloud condensation nuclei properties at a polluted site in southeastern China during the AMF-China campaign, *J. Geophys. Res.*, *116*, D00K35, doi:10.1029/2011JD016395.

Liu, J., Y. Zheng, Z. Li, C. Flynn, E. J. Welton, and M. Cribb (2011b), Transport, vertical structure and radiative properties of dust events in southeast China determined from ground and space sensors, *Atmos. Environ.*, *45*(35), 6469–6480.

Liu, J., Y. Zheng, Z. Li, C. Flynn, and M. Cribb (2012), Seasonal variations of aerosol optical properties, vertical distribution and associated radiative effects in the Yangtze Delta region of China, *J. Geophys. Res.*, *117*, D00K38, doi:10.1029/2011JD016490.

Lohmann, U., and J. Feichter (2005), Global indirect aerosol effects: A review, *Atmos. Chem. Phys.*, *5*, 715–737.

Nakajima, T., G. Tonna, R. Rao, Y. Kaufman, and B. Holben (1996), Use of sky brightness measurements from ground for remote sensing of particulate polydispersions, *Appl. Opt.*, *35*, 2672–2686.

Nakajima, T., et al. (2003), Significance of direct and indirect radiative forcings of aerosols in the East China Sea region, *J. Geophys. Res.*, *108*(D23), 8658, doi:10.1029/2002JD003261.

Nakajima, T., et al. (2007), Overview of the ABC EAREX 2005 regional experiment and a study of the aerosol direct radiative forcing in East Asia, *J. Geophys. Res.*, *112*, D24S91, doi:10.1029/2007JD009009.

O'Brien, D. M., and R. M. Mitchell (2003), Atmospheric heating due to carbonaceous aerosol in northern Australia—Confidence limits based on TOMS aerosol index and sun-photometer data, *Atmos. Res.*, *66*, 21–41.

Ramanathan, V., P. J. Crutzen, J. T. Kiehl, and D. Rosenfeld (2001a), Aerosol, climate, and hydrological cycle, *Science*, *294*, 2119–2124.

Ramanathan, V., et al. (2001b), Indian Ocean experiment: An integrated analysis of the climate forcing and effects of the great Indo-Asian haze, *J. Geophys. Res.*, *106*, 28,371–28,398, doi:10.1029/2001JD900133.

Ramanathan, V., C. Chung, D. Kim, T. Bettge, L. Buja, J. T. Kiehl, W. M. Washington, Q. Fu, D. R. Sikka, and M. Wild (2005), Atmospheric brown clouds: Impacts on South Asian climate and hydrological cycle, *Proc. Natl. Acad. Sci. U. S. A.*, *102*, 5326–5333, doi:10.1073/pnas.0500656102.

Ramanathan, V., et al. (2008), *Atmospheric Brown Clouds and Regional Climate Change, Part I of Atmospheric Brown Clouds: Regional Assessment Report With Focus on Asia*, Project Atmospheric Brown Cloud, United National Environment Programme, Nairobi, Kenya.

Takamura, T., N. Sugimoto, A. Shimizu, A. Uchiyama, A. Yamazaki, K. Aoki, T. Nakajima, B. J. Sohn, and H. Takenaka (2008), Aerosol radiative characteristics at Gosan, Korea, during the Atmospheric Brown Cloud East Asian Regional Experiment 2005, *J. Geophys. Res.*, *112*, D22S36, doi:10.1029/2007JD008506.

Tsai, F., G. T.-J. Chen, T.-H. Liu, W.-D. Lin, and J.-Y. Tu (2008), Characterizing the transport pathways of Asian dust, *J. Geophys. Res.*, *113*, D17311, doi:10.1029/2007JD009674.

Uchiyama, A., A. Yamazaki, H. Togawa, and J. Asano (2005), Characteristics of aeolian dust observed by sky-radiometer in the Intensive Observation Period 1 (IOP1), *J. Meteorol. Soc. Jpn.*, *83A*, 291–305.

Wu, D., J. Zhou, D. Liu, Z. Wang, Z. Zhong, C. Xie, F. Qi, A. Fan, and Y. Wang (2011), 12-year LIDAR observations of tropospheric aerosol over Hefei (31.9°N, 117.2°E), China, *J. Opt. Soc. Korea*, *15*, 90–95.

Xia, X., C. Hongbin, and W. Pucai (2004), Aerosol properties in a Chinese semiarid region, *Atmos. Environ.*, *38*, 4571–4581.

Xia, X., C. Hong-Bin, W. Pu-Cai, Z. Xue-Mei, Q. Jin-Huan, and P. Gouloub (2005), Aerosol properties and their spatial and temporal variations over North China in spring 2001, *Tellus, Ser. B*, *57*, 28–39, doi:10.1111/j.1600-0889.2005.00126.x.

Xia, X., Z. Li, B. Holben, P. Wang, T. Eck, H. Chen, M. Cribb, and Y. Zhao (2007a), Aerosol optical properties and radiative effects in the Yangtze Delta region of China, *J. Geophys. Res.*, *112*, D22S12, doi:10.1029/2007JD008859.

Xia, X., H. Chen, Z. Li, P. Wang, and J. Wang (2007b), Significant reduction of surface solar irradiance induced by aerosols in a suburban region in northeastern China, *J. Geophys. Res.*, *112*, D22S02, doi:10.1029/2006JD007562.

Xia, X., Z. Li, P. Wang, H. Chen, and M. Cribb (2007c), Estimation of aerosol effects on surface irradiance based on measurements and radiative transfer model simulations in northern China, *J. Geophys. Res.*, *112*, D22S10, doi:10.1029/2006JD008337.

Xin, J., et al. (2007), Aerosol optical depth (AOD) and Ångström exponent of aerosols observed by the Chinese Sun Hazemeter Network from August 2004 to September 2005, *J. Geophys. Res.*, *112*, D05203, doi:10.1029/2006JD007075.

Xu, J., M. H. Bergin, X. Yu, G. Liu, J. Zhao, C. M. Carrico, and K. Baumann (2002), Measurement of aerosol chemical, physical and radiative properties in the Yangtze delta region of China, *Atmos. Environ.*, *36*, 161–173.

Yu, H., et al. (2006), A review of measurement-based assessments of the aerosol direct radiative effect and forcing, *Atmos. Chem. Phys.*, *6*, 613–666.

Yu, X., B. Zhu, Y. Yin, S. X. Fan, and A. J. Chen (2011), Seasonal variation of columnar aerosol optical properties in Yangtze River Delta in China, *Adv. Atmos. Sci.*, *28*(6), 1326–1335, doi:10.1007/s00376-011-0158-9.

Zege, E. P., A. P. Ivanov, and I. L. Katsev (1991), *Image Transfer Through a Scattering Medium*, Springer-Verlag, New York.

Zheng, Y., J. Liu, R. Wu, Z. Li, B. Wang, and T. Tamio (2008), Seasonal statistical characteristics of aerosol optical properties at a site near a dust region in China, *J. Geophys. Res.*, *113*, D16205, doi:10.1029/2007JD009384.

Zhou, J., G. Yu, C. Jin, F. Qi, D. Liu, H. Hu, Z. Gong, G. Shi, T. Nakajima, and T. Takamura (2002), Lidar observations of Asian dust over Hefei, China, in spring 2000, *J. Geophys. Res.*, *107*(D15), 4252, doi:10.1029/2001JD000802.